metals

MDPI

Article

Effects of Solid-Solution Carbon and Eutectic Carbides in AISI 316L Steel-Based Tungsten Carbide Composites on Plasma Carburizing and Nitriding

Shinichiro Adachi *, Takuto Yamaguchi, Keigo Tanaka, Takashi Nishimura and Nobuhiro Ueda

Osaka Research Institute of Industrial Science and Technology, 2-7-1 Ayumino, Izumi 594-1157, Osaka, Japan
* Correspondence: shinadachi@orist.jp; Tel.: +81-725-51-2648; Fax: +81-725-51-2749

Abstract: AISI 316L stainless-steel-based tungsten carbide composite layers fabricated via laser metal deposition are used for additive manufacturing. Heat treatment practices such as low-temperature plasma carburizing and nitriding improve the hardness and corrosion resistance of austenitic stainless steels via the formation of expanded austenite, known as the S phase. In the present study, practices to enhance the hardness and corrosion resistances of the stainless-steel parts in the composite layers have been investigated, including single plasma carburizing for 4 h and continuous plasma nitriding for 3.5 h following carburizing for 0.5 h at 400 and 450 °C. The as-deposited composite layers contain solid-solution carbon and eutectic carbides owing to the thermal decomposition of tungsten carbide during the laser metal deposition. The eutectic carbides inhibit carbon diffusion, whereas the original solid-solution carbon contributes to the formation of the S phase, resulting in a thick S phase layer. Both the single carburizing and continuous processes are effective in improving the Vickers surface hardness and corrosion resistance of the composite layers despite containing the solid-solution carbon and eutectic carbides.

Keywords: plasma carburizing; plasma nitriding; laser metal deposition; stainless steel; tungsten carbide; hardness; corrosion resistance

check for updates

Citation: Adachi, S.; Yamaguchi, T.; Tanaka, K.; Nishimura, T.; Ueda, N. Effects of Solid-Solution Carbon and Eutectic Carbides in AISI 316L Steel-Based Tungsten Carbide Composites on Plasma Carburizing and Nitriding. *Metals* **2023**, *13*, 1350. https://doi.org/10.3390/met13081350

Academic Editor: Catalin Constantinescu

Received: 21 June 2023
Revised: 20 July 2023
Accepted: 25 July 2023
Published: 27 July 2023

Copyright: © 2023 by the authors. Licensee MDPI, Basel, Switzerland. This article is an open access article distributed under the terms and conditions of the Creative Commons Attribution (CC BY) license (https://creativecommons.org/licenses/by/4.0/).

1. Introduction

Additive manufacturing using molten metal and laser-beam heating is widely used for the fabrication of three-dimensional objects, particularly parts with complex shapes or highly functional materials that are difficult to machine. Recently, additive manufacturing technology has been rapidly developed and is now applied in the aerospace industry and medical field, as well as to fabricate general prototypes and machinery parts. Additive manufacturing includes methods such as directed energy deposition, whereby a molten metal powder or wire is deposited on a substrate to form an object via repeated layering, and powder bed fusion, wherein a laser beam is repeatedly irradiated onto a bed of powder to form an object [1–6].

Steel materials, particularly austenitic stainless steels such as AISI 316L, which are readily available and exhibit excellent corrosion resistance, are actively used for additive manufacturing. The metallurgical and mechanical properties of additively manufactured AISI 316L stainless steels have been extensively studied [7–13]. Additive manufacturing via laser metal deposition has been used to improve the wear resistance of stainless-steel materials via compositing with tungsten carbide particles [14–18]. Tungsten carbide can improve the hardness of stainless-steel materials via dispersion. Furthermore, eutectic carbides are formed by the reaction of pyrolyzed tungsten carbide particles with the metal elements in stainless steel; these eutectic carbides enhance the hardness of stainless steel. However, unlike hard materials, such as ceramics and cermet materials, the stainless-steel parts in tungsten carbide composite layers cannot withstand severe friction and wear environments.

Low-temperature nitriding of austenitic stainless steels at temperatures below 450 °C supersaturates the nitrogen atoms in the austenite crystal lattice, thereby forming an expanded austenite phase, namely the S phase, which improves their hardness and wear resistance. The S phase is a solid solution of nitrogen (not a nitride compound), which does not affect the passive-film-forming ability of chromium in stainless steel. Thus, high corrosion resistance is maintained, and pitting corrosion in chlorinated environments is inhibited [19–28]. In a previous study, AISI 316L stainless-steel-based tungsten carbide composite layers fabricated via laser metal deposition were subjected to low-temperature plasma nitriding, and the formation of the S phase was confirmed at temperatures of 400–450 °C and a processing time of 4 h [29]. The hardness of the stainless-steel parts in the composite layers increased from 500–700 HV to 1200–1400 HV. The as-deposited composite layers exhibited poor corrosion resistance in NaCl because the solid-solution chromium formed eutectic carbides and weakened the passive film. However, the plasma nitriding treatment significantly increased the pitting resistance equivalent number (PREN) with the dissolution of nitrogen, and consequently, the corrosion resistance of the composite layers increased. In addition, the metallurgical structure of the composite layers was significantly different from that of general stainless-steel materials. Solid-solution carbon was produced by the thermal decomposition of the tungsten carbide particles during the laser metal deposition. The composite layers, when subjected to low-temperature plasma nitriding, formed a dual S phase layer, i.e., a supersaturated nitrogen S phase (nitriding S phase) on the outside and a supersaturated carbon S phase (carburizing S phase) inside. These results suggest that the original solid-solution carbon played a major role in the formation of the S phase.

Low-temperature carburizing of stainless-steel materials using carburizing gases, such as methane, propane, and butane, is a common method for producing a carburizing S phase with supersaturated carbon. In this method, carbon diffuses from the surface to form an expanded austenitic phase, thus improving wear resistance similar to the nitriding S phase [30–37]. Furthermore, compared to only carburizing or nitriding, a continuous or simultaneous treatment that combines carburizing and nitriding can increase the thickness, hardness, and wear resistance of the S phase [38–45]. Therefore, low-temperature carburizing and combined treatments for AISI 316L stainless-steel-based tungsten carbide composite layers can be used to improve wear and corrosion resistance.

A few papers have reported low-temperature nitriding and carburizing for austenitic stainless-steel fabrication via directed energy deposition and powder bed fusion [22,24,32,46,47]. However, to the best of our knowledge, none of the studies published to date investigate tungsten carbide composites except the previous study [29]. The effect of original solid-solution carbon present in stainless-steel plates on low-temperature nitriding has been well-researched in previous studies, establishing the formation of thin carburizing S phase layers at the interface between the nitriding layer and substrate [21,26,48,49]. In contrast, the effect on low-temperature carburizing has not been investigated yet because the amount of original solid-solution carbon in stainless-steel materials is negligible compared with that of carbon diffused via carburizing. However, AISI 316L stainless-steel-based tungsten carbide composite layers contain large amounts of solid-solution carbon and eutectic carbides; therefore, their effect on the S phase cannot be ignored, unlike that in ordinary stainless-steel plates. Moreover, the original solid-solution carbon in the composite layers can influence the formation and properties of the carburizing S phase more than those of the nitriding S phase because the diffusing element is carbon.

In this study, AISI 316L stainless-steel-based tungsten carbide composite layers were fabricated via laser metal deposition and followed by treatment with two methods, a single plasma carburizing process, and a continuous plasma nitriding process after carburizing at temperatures below 450 °C. The microstructure, X-ray diffraction (XRD) patterns, and depth profiles of carbon and nitrogen were examined to reveal the formation mechanism of the S phase and evaluate the influence of the original solid-solution carbon and eutectic carbides. In addition, the S phase properties were evaluated via Vickers hardness and

anodic polarization measurements. The effects of the tungsten carbide composition and plasma process conditions were investigated to develop the optimal treatment method for the composite layers.

2. Experimental Section

Composite layers of AISI 316L stainless-steel-based tungsten carbide with a thickness of approximately 2 mm were fabricated using a laser metal deposition machine equipped with a continuous-wave diode laser (wavelength, 940 nm; LDM-2000-60, Laserline, GmbH, Mulheim-Karlich, Germany) and attached coaxial powder feed head (COAX12, Fraunhofer, Munchen, Germany). The output power of the laser beam was 1.4 kW, and a single layer was deposited on the AISI 304 stainless-steel plates with a size of 65 mm × 65 mm × 10 mm and a composition of 0.04 wt.% C, 0.3 wt.% Si, 1.7 wt.% Mn, 0.04 wt.% P, 0.01 wt.% S, 8.5 wt.% Ni, 18.2 wt.% Cr and Fe (balance) by scanning the coaxial powder feed head at a transverse speed of 4 mm s^{-1} and length of 50 mm at 3 mm intervals. The AISI 316L stainless-steel powder with a particle size of −212/+63 μm and a composition of 0.03 wt.% C, 0.7 wt.% Si, 0.9 wt.% Mn, 0.03 wt.% P, 0.02 wt.% S, 12.4 wt.% Ni, 17.4 wt.% Cr, 2.1 wt.% Mo and Fe (balance) was mixed with 20 and 40 wt.% tungsten carbide powder with a particle size of −180/+53 μm and a carbon content of about 5 wt.%, which was delivered in the coaxial direction of the laser beam through the powder feed head with mass flow rates of 17–19 g min^{-1}; Ar was used as the carrier gas.

The low-temperature plasma treatments at 400 and 450 °C were performed using two processes: single carburizing for 4 h and continuous nitriding for 3.5 h after carburizing for 0.5 h, using a DC plasma ion treatment machine (FECH-1N, Fuji Electronics Industry, Osaka, Japan). Before the plasma treatments, the surfaces of the composite layers were polished to remove any oxide layer and flattened like a mirror because an oxide layer prevents the diffusion of carbon and nitrogen. The polished samples and a copper plate in a glass chamber were connected to the cathode and anode electrodes, respectively. CH_4:Ar:H_2 (5:50:45) and N_2:H_2 (80:20) with a flow rate of 1 L min^{-1} were used as the plasma gases in the chamber to maintain the pressure at 667 Pa for the carburizing and nitriding processes, respectively. The crystal structure was examined using XRD (SmartLab, Rigaku, Tokyo, Japan) via a conventional θ–2θ scan of Cu-Kα radiation at 40 kV and 150 mA with a scan rate of 10-degree min^{-1}. Compounds were identified from XRD peaks using the JCPDS cards. The cross-sectional microstructure was observed using an optical microscope (ECLIPSE MA100N; Nikon, Tokyo, Japan). The depth profiles of carbon and nitrogen were examined through glow-discharge optical emission spectroscopy (GDOES; GDA750 system Rigaku, Tokyo, Japan). The surface atomic composition was evaluated using X-ray photoelectron spectroscopy (XPS; PHI Quantera II instrument, Ulvac-PHI, Kanagawa, Japan). The XPS data was collected by a monochromatic Al Kα radiation with an X-ray beam diameter of 200 μm. Ar^+ was used for the sputtering with a rate of 2 nm min^{-1} for the oxide layer of SiO_2.

The surface hardness of the stainless-steel parts of the composite layers was measured using a Vickers tester (HM-220D, Mitutoyo, Tokyo, Japan) with a test load of 0.245 N. The Vickers tests were repeated at least eight times for each sample, and the maximum and minimum values were deleted. The hardness depth profiles of the cross-sections were measured using a nanoindentation tester (ENT-1100a, Elionix, Tokyo, Japan) with a test load of 1 mN and a loading rate of 1×10^{-4} N s^{-1}. The nanoindentation tests were repeated four times, and the data with an indentation depth of less than 50 nm were deleted.

The anodic polarization curves were obtained using a potentiostat (HSV-110, Hokuto Denko Corporation, Tokyo, Japan) with an Ag/AgCl reference electrode and platinum wire counter electrode. The samples were directly exposed to polarization tests, and the measurement voltage was applied between −0.6 V and 1 V with a scan rate of 1 mV s^{-1}—a 3.5 wt.% NaCl solution at a temperature of 30 °C was used for the measurements. Since the dissolved oxygen in the solution may affect the polarization curves, oxygen was removed by bubbling nitrogen gas for at least 0.5 h prior to the measurements. After the measurements,

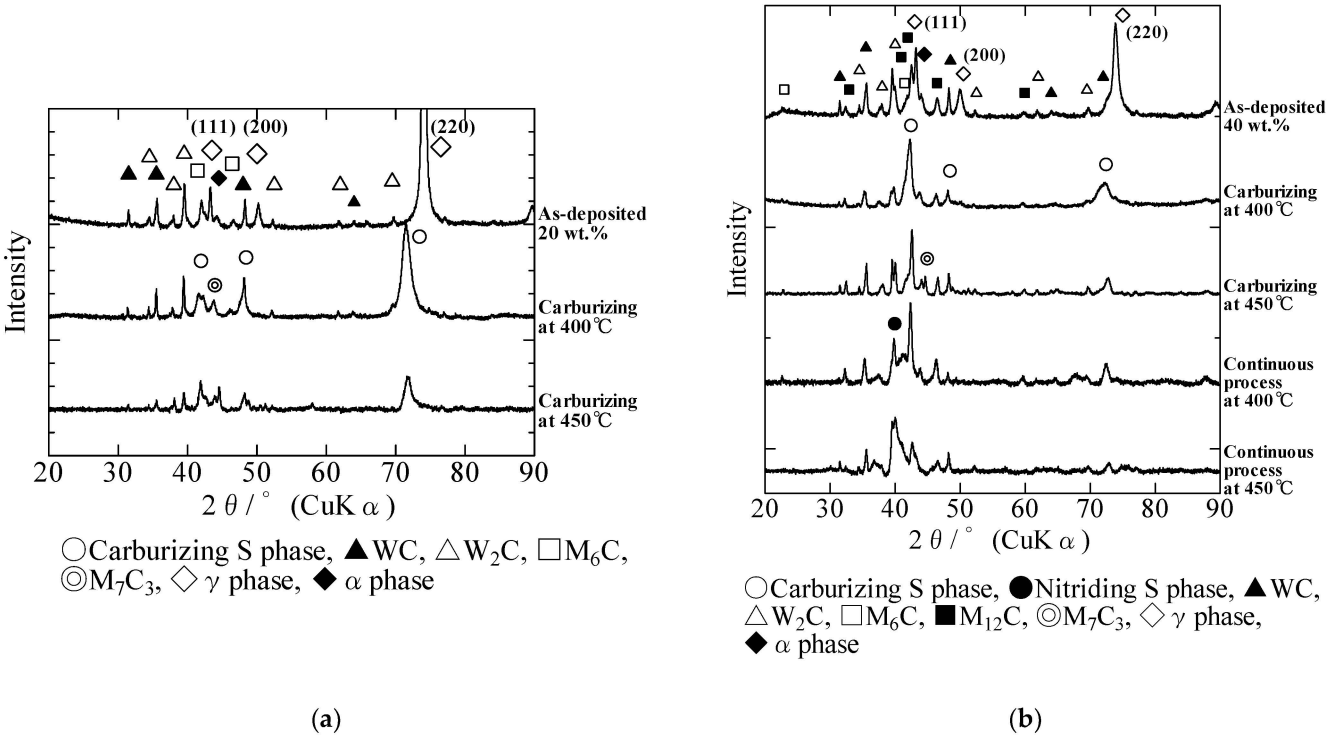
the surface morphologies were examined using a digital microscope (Dino-Lite, AnMo Electronics Corporation, Taipei, Taiwan).

3. Results and Discussion

3.1. Formation Mechanism of the S Phase during a Single Carburizing Process

Figure 1 shows the XRD patterns of the AISI 316L stainless-steel-based tungsten carbide composite layers. The as-deposited composite layers contained the austenite (γ) and a small amount of ferrite (α) phase in stainless steel with the eutectic carbides WC, W_2C, and M_6C. $M_{12}C$ was found only in the 40 wt.% tungsten carbide layer. After the single carburizing process had been conducted for 4 h, the diffraction peaks of the austenite phase shifted to lower angles. The etched cross-sectional microstructure in Figure 2 shows bright-contrast layers on the surface. These results indicate that the crystal lattice of the austenite phase was expanded by the supersaturated solid solution of carbon, that is, the S phase formed on the composite layers.

Figure 3 shows the S phase thickness obtained by measuring the bright-contrast layer thickness, as shown in Figure 2. The average S phase thicknesses of the 20 wt.% composite layers with single carburizing temperatures of 400 and 450 °C were 7.3 and 19.9 μm respectively, and those of the 40 wt.% composite layers were 7 and 14.5 μm respectively. Figure 4a,b show the depth profiles of carbon obtained by GDOES. As indicated by the arrows, the carbon content in the 20 wt.% composite layers increased at depths of 9 and 21 μm, respectively, at 400 and 450 °C, whereas the carbon content in the 40 wt.% composite layers increased at depths of 8.5 and 15.5 μm, respectively. These depths with increased carbon contents were marginally larger than the thickness of the S phase (difference of less than 2 μm) for both 20 and 40 wt.% composite layers. Considering that eutectic carbide existed in the as-deposited composite layers, high content of the original solid-solution carbon was expected before the carburizing process. Therefore, only a slight increase in the solid-solution carbon content due to the carburizing process can immediately lead to the formation of the S phase.



(**a**) (**b**)

Figure 1. XRD patterns of the AISI 316L steel-based composite layers at tungsten carbide composition of (**a**) 20 wt.% and (**b**) 40 wt.%.

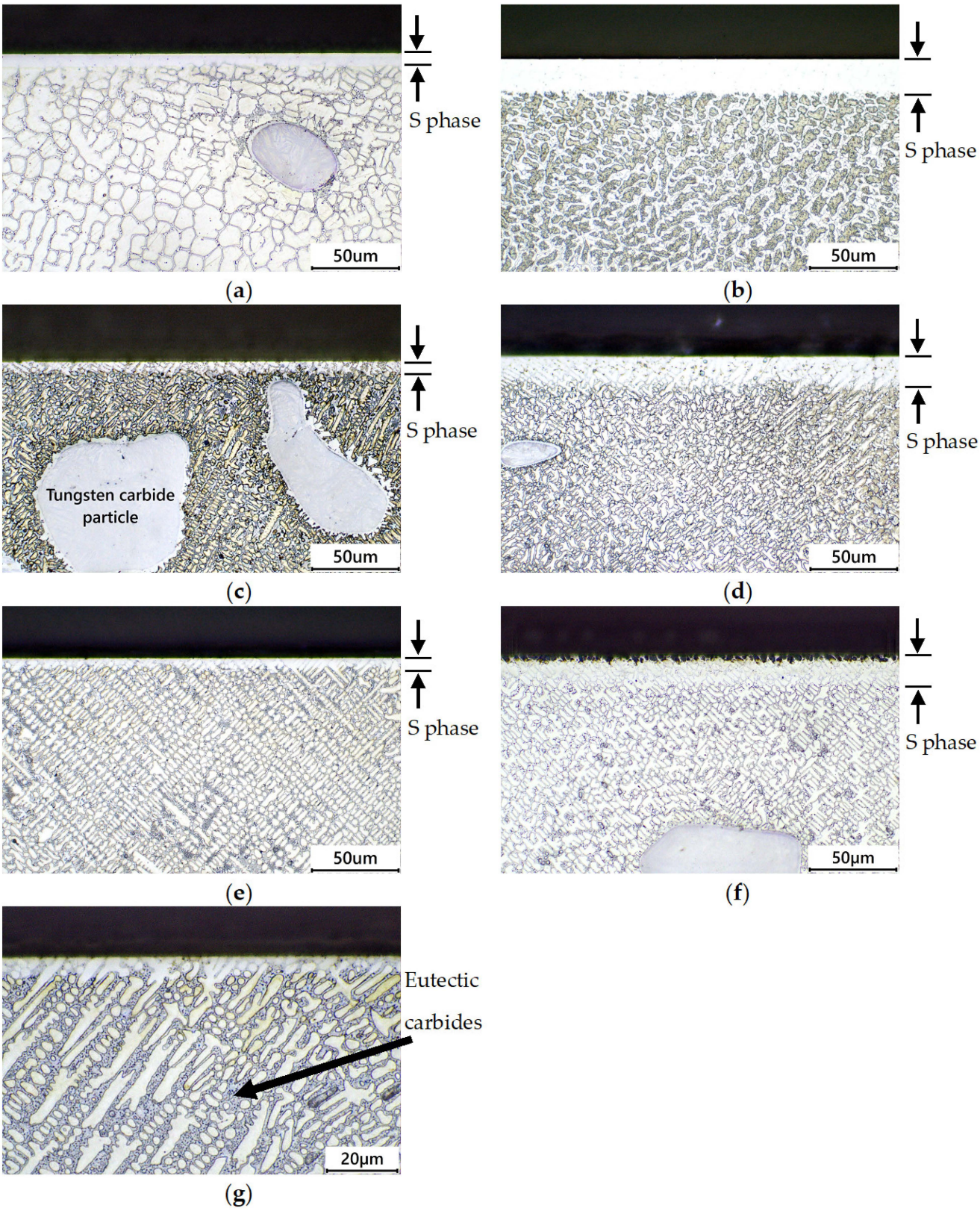


Figure 2. Cross-sectional micrographs of the AISI 316L steel-based composite layers obtained after the plasma processes at tungsten carbide compositions of (**a**) 20 wt.% carburized at 400 °C, (**b**) 20 wt.% carburized at 450 °C, (**c**) 40 wt.% carburized at 400 °C, (**d**) 40 wt.% carburized at 450 °C, (**e**) 40 wt.% continuously processed at 400 °C, (**f**) 40 wt.% continuously processed at 450 °C, and (**g**) enlarged view of 40 wt.% continuously processed at 400 °C.

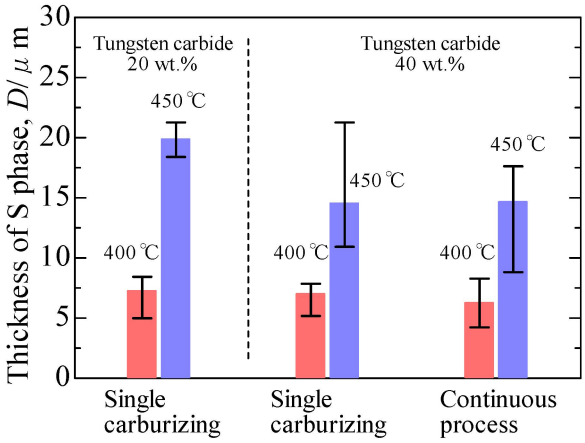


Figure 3. Thickness of the S phase on the AISI 316L steel-based composite layers at various tungsten carbide compositions after the plasma processes.

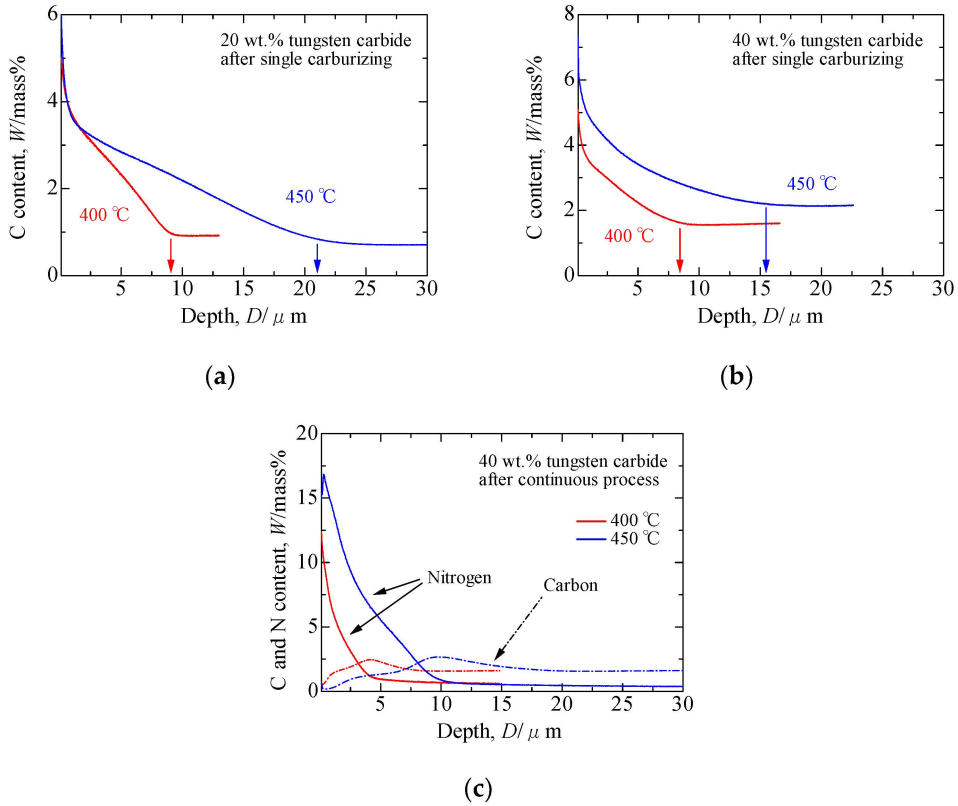


Figure 4. Carbon and nitrogen depth profiles of the AISI 316L steel-based composite layers after the plasma processes at tungsten carbide compositions of (**a**) 20 wt.% after carburizing, (**b**) 40 wt.% after carburizing, and (**c**) 40 wt.% after continuous process.

The depth profiles of carbon exhibit a smooth downward trend in general carburizing treatments [50]. This shape possibly originates from the dissolved chromium, which restricts carbon diffusion in stainless steel with binding carbon [51]. Figure 4a shows that a decrease in carbon content in the 20 wt.% composite layers follows a typical S phase profile. In contrast, in the 40 wt.% composite layers, the carbon content gradually decreases toward the interior, according to Fick's second law of diffusion (Figure 4b). This implies that the synthesis of eutectic carbides, such as M_6C and $M_{12}C$, in the as-deposited composite layers reduced the dissolved chromium content. Because the original solid-solution carbon is already bound to the dissolved chromium, its restriction on carbon diffusion weakens.

However, eutectic carbides can inhibit carbon diffusion. The XRD pattern in Figure 1 shows that the M_7C_3 carbide was formed by the single carburizing process. A prolonged low-temperature gas-phase carburizing of the AISI 316L stainless steel can cause the intragranular precipitation of M_7C_3 [52]. In this study, the diffused carbon was trapped by the eutectic carbides M_6C and $M_{12}C$, and the trapped carbon formed M_7C_3, with a high carbon equivalent, via the following reactions:

$$7M_{12}C + 29C \rightarrow 12M_7C_3, \quad (1)$$

$$7M_6C + 11C \rightarrow 6M_7C_3. \quad (2)$$

As shown in Figure 2g, the gray areas of the microstructure are eutectic carbides. Figure 2a–f reveals the presence of eutectic carbides as dendrite-like metallographic structures inside the composite layers. Evidently, the size of the equiaxed grains (equiaxed crystals) in the dendritic structures in the 40 wt.% composite layers is smaller than that of grains in the 20 wt.% composite layers. This result indicates that more densely distributed eutectic carbides were formed because of the higher tungsten carbide composition. The S phase in the 40 wt.% composite layer at 450 °C is thinner than that in the 20 wt.% layer (Figure 3). Further, carbon diffusion in the 40 wt.% composite layer at 450 °C is shallower than in the 20 wt.% composite layer (Figure 4). These results suggest that the eutectic carbides act as carbon diffusion barriers. In addition, no difference in the thickness of the S phase at 400 °C is observed. This suggests that the effect of the eutectic carbides could be negligible at 400 °C because the diffusion rate at 400 °C is slower than at 450 °C. However, the thickness of the S phase in the composite layers was larger than that on AISI 316L steel plate (12 μm) after 4 h plasma carburizing at 450 °C [37]. This was attributed to the original solid-solution carbon contributing to the formation of the S phase, thus resulting in a thick S phase layer.

3.2. Formation Mechanism of the S Phase during a Continuous Plasma Nitriding after Carburizing Process

Figure 1b shows the XRD patterns of the 40 wt.% tungsten carbide layers obtained by continuous nitriding for 3.5 h after carburizing for 0.5 h, thus indicating the coexistence of the supersaturated carbon S phase (carburizing S phase) and nitrogen S phase (nitriding S phase). Nitrogen in the S phase has a higher solubility concentration than carbon in the S phase, thus resulting in a greater expansion of the austenite lattice [53,54]. Therefore, the diffraction peaks of the nitriding S phase (111) shift to a lower angle than those of the carburizing S phase. In addition, in the carbon depth profiles (Figure 4c), the carbon peaks are located in a deeper region compared with the nitrogen peaks, suggesting that the nitriding S phase developed on the outside, whereas the carburizing S phase formed on the inside. Note that the diffusion rate of carbon in the austenite phase is higher than that of nitrogen [55], and the affinity of the dissolved chromium to trap nitrogen is greater than that for carbon [56]; therefore, carbon was pushed inside by the diffused nitrogen. Consequently, the S phase exhibited a dual structure. The pushed carbon included the carbon diffused during the first carburizing process and the original solid-solution carbon, similar to the single carburizing process.

Figure 3 shows that the thickness of the dual S phase is 6.3 μm at 400 °C and 14.7 μm at 450 °C, which is similar to that of the S phase formed by the single carburizing process. Notably, a continuous process combining carburizing and nitriding for austenitic stainless-steel plates increases the thickness of the S phase [38–45]. However, in this study, the amount of carbon increased during the first carburizing, which was conducted for a short time of 0.5 h in the continuous process and was less than the original solid-solution carbon content. Therefore, the thickness of the S phase increased only negligibly during the first carburizing process.

3.3. Hardness of the S Phase by a Single Carburizing Process and Continuous Nitriding after Carburizing Process

The surface hardness of the S phase in the stainless-steel parts was measured using the Vickers hardness test, and the results are shown in Figure 5. The average hardness values of the samples treated by the single carburizing process at 400 and 450 °C for the 20 wt.% layers are 1342 and 1330 HV, respectively, whereas those for the 40 wt.% composite layers are 1210 and 1365 HV, respectively. With the continuous nitriding process after carburizing, the 40 wt.% composite layers exhibit surface hardness values of 1312 and 1361 HV at 400 and 450 °C, respectively. The average hardness of the as-deposited layers is 504 HV and 647 HV for the 20 wt.% and 40 wt.% composite layers, respectively, indicating that the formation of the S phase increases the hardness values. On the other hand, the surface hardness values corresponding to the different tungsten carbide compositions remained almost the same for the single carburizing and continuous processes.

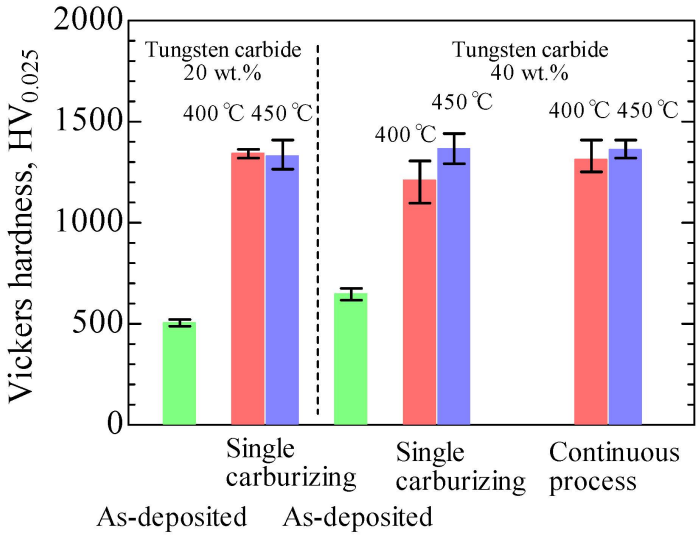


Figure 5. Vickers surface hardness of the AISI 316L steel-based composite layers with various tungsten carbide compositions.

Figure 6 shows the surface hardness profiles of the S phase processed at 450 °C, demonstrating that the S phase resulting from the continuous process was harder than that produced by the single carburizing process up to a depth of approximately 4 μm. The XRD pattern in Figure 1 shows that the peak of (111) associated with the nitrided S phase shifted to a lower angle compared with that of the carburized S phase. Additionally, the GDOES results displayed in Figure 4 indicate that the nitrogen content in the near-surface area up to a depth of 5 μm during the continuous process was 5–16 wt.%, whereas the carbon content after the single carburizing process was comparatively low (3–6 wt.%). This result indicates that the solid-solution nitrogen content obtained from the nitriding in the continuous process is higher than the carbon content from the single carburizing process. Consequently, the near surface of the S phase, produced by the continuous process, exhibited enhanced hardness.

The hardness depth profiles in Figure 6 show that the hardness values of the 40 wt.% layers are 9 GPa in the deep region where the S phase was not formed. The hardness values are higher than the 20 wt.% composite layer values of 6 GPa. The original solid-solution carbon and eutectic carbide concentrations in the 40 wt.% composite layers are higher than those in the 20 wt.% composite layers, which may have resulted in the enhanced hardness of the stainless-steel parts.

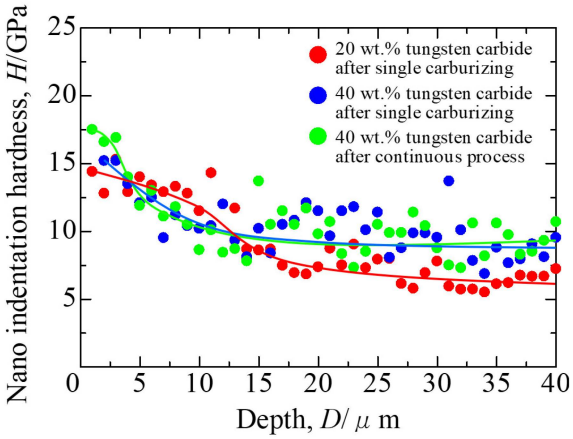
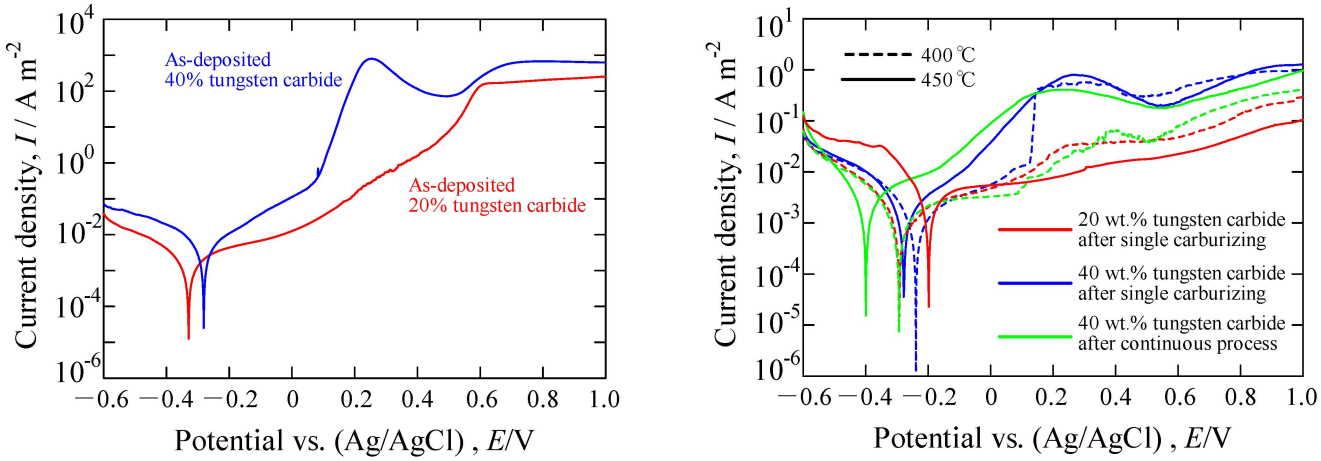


Figure 6. Hardness depth profiles of the AISI 316L steel-based composite layers with various tungsten carbide compositions treated via different plasma processes at 450 °C.

3.4. Anodic Polarization Measurement of the S Phase by a Single Carburizing Process and Continuous Nitriding after Carburizing Process

The anodic polarization measurements were conducted in a 3.5 wt.% NaCl solution. Table 1 shows the corrosion potential and current density from the polarization curves in Figure 7. The corrosion current densities of the as-deposited layers are slightly larger than those of the plasma-processed layers with the same tungsten carbide composition except for the 20 wt.% layer carburized at 450 °C. When the potential is above 0.6 V, the current densities of the as-deposited layers are 100 A m^{-2}, but those of the plasma-processed layers are less than 1 A m^{-2}. Figure 8 shows the surface morphologies after the anodic polarization measurements. The pitting and crevice corrosion is observed around the boundary of the tested area in the as-deposited layers of (a) and (b), especially the 40 wt.% layer was severely corroded. Although some discoloration is observed in the plasma-processed layers of (c)–(h), no sever corrosion is evident, confirming the high corrosion resistance of the S phase on the composite layers. In the continuous process, the nitriding S phase was formed at the surface. Moreover, as nitrogen dissolved in stainless steel strongly increases the PREN [29], the S phase produced by the continuous process suppresses sever pitting corrosion.



(**a**) (**b**)

Figure 7. Anodic polarization curves of the AISI 316L steel-based composite layers with various tungsten carbide compositions of (**a**) as-deposited and (**b**) treated various plasma processes.

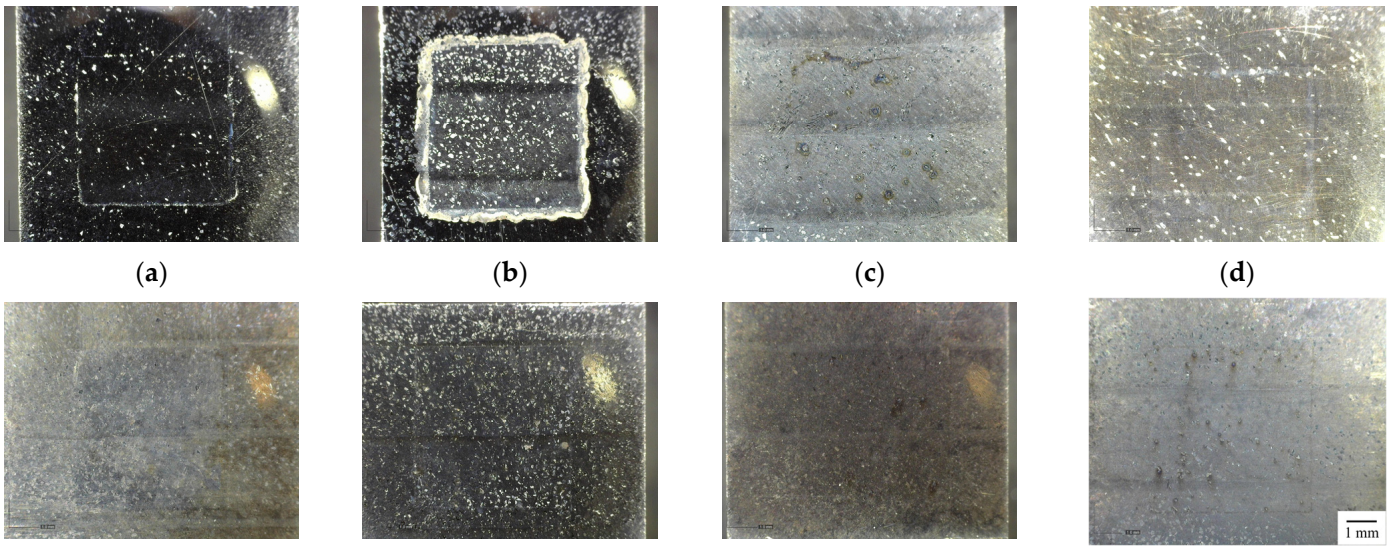


Figure 8. Surface morphologies of the AISI 316L steel-based composite layers with various tungsten carbide compositions after the anodic polarization measurements of (**a**) 20 wt.% as-deposited, (**b**) 40 wt.% as-deposited, (**c**) 20 wt.% carburized at 400 °C, (**d**) 20 wt.% carburized at 450 °C, (**e**) 40 wt.% carburized at 400 °C, (**f**) 40 wt.% carburized at 450 °C, (**g**) 40 wt.% continuously processed at 400 °C, and (**h**) 40 wt.% continuously processed at 450 °C.

Table 1. Corrosion potential and current density in the anodic polarization curves of the AISI 316L steel-based composite layers.

Sample	Corrosion Potential	Corrosion Current Density
	(V)	(A m^{-2})
20 wt.% as-deposited	−0.33	2.0×10^{-3}
40 wt.% as-deposited	−0.28	4.4×10^{-3}
20 wt.% carburized at 400 °C	−0.29	1.5×10^{-3}
20 wt.% carburized at 450 °C	−0.20	4.1×10^{-3}
40 wt.% carburized at 400 °C	−0.24	1.7×10^{-3}
40 wt.% carburized at 450 °C	−0.28	1.8×10^{-3}
40 wt.% continuously processed at 400 °C	−0.29	2.2×10^{-3}
40 wt.% continuously processed at 450 °C	−0.40	3.8×10^{-3}

Figure 9 shows the depth profiles of the atomic concentrations obtained by XPS. The spectrum of the as-deposited 40 wt.% layer surface exhibits an oxygen peak with a low-intensity chromium peak, suggesting the presence of a passive film. The spectrum of the S phase in the 40 wt.% composite layer treated with the single carburizing process at 450 °C also exhibits an oxygen peak with a low-intensity chromium peak, indicating that although sever pitting corrosion is suppressed, a strong passive film is not formed. Low-temperature carburizing reportedly improves pitting corrosion resistance. This implies that instead of the passive film, the S phase containing dissolved excess carbon inhibited the pitting corrosion [50,57,58]. Therefore, the suppression of sever pitting corrosion in the composite layers treated by the single carburizing process can also be attributed to the supersaturated carbon S phase.

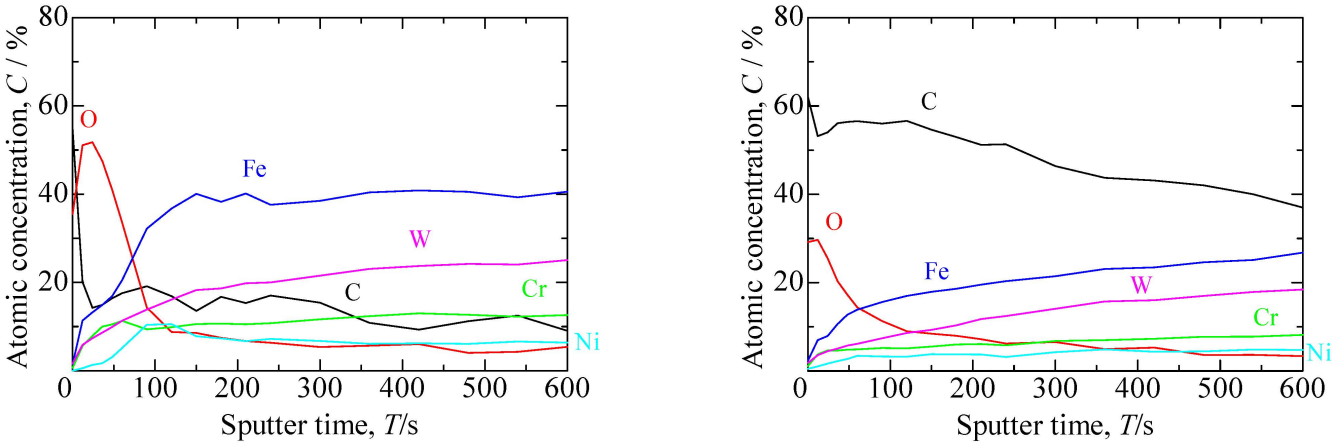


Figure 9. XPS depth profiles of carbon, oxygen, chromium, iron, nickel, and tungsten in the 40 wt.% tungsten carbide composite layers: (**a**) as-deposited and (**b**) carburized at 450 °C.

It should be noted that the corrosion current densities of the plasma-processed layers in Figure 7b do not exhibit any distinct difference or trend with varying tungsten carbide composition or plasma process conditions. Therefore, it is difficult to determine which plasma process condition is most effective for corrosion resistance.

4. Conclusions

In this study, AISI 316L stainless-steel-based tungsten carbide composite layers were fabricated via laser metal deposition and treated with single carburizing for 4 h and continuous nitriding for 3.5 h after carburizing for 0.5 h at 400 and 450 °C to form an expanded austenite phase (S phase). The formation mechanism of the S phase was investigated considering the influence of the original solid-solution carbon and eutectic carbides, which were produced by the thermal decomposition of the tungsten carbide particles during the laser metal deposition process. In addition, the hardness and anodic polarization (in a NaCl solution) of the S phase were evaluated depending on the tungsten carbide composition and plasma treatment conditions.

(1) In the single carburizing process, the S phase was formed with the addition of diffused carbon to the solid-solution carbon originally present in the composite layers. The eutectic carbides in the as-deposited composite layers prevented carbon diffusion, and the S phase in the 40 wt.% composite layers, which included more eutectic carbides, was thinner than that in the 20 wt.% composite layers. However, the original solid-solution carbon was involved in the formation of the S phase. Therefore, the thickness of the S phase layer in the composites was higher than that of the S phase on the AISI 316L stainless-steel plates.

(2) In the continuous process, the first carburizing step induced carbon diffusion, and the diffused carbon and original solid-solution carbon were pushed inside by the diffused nitrogen during the second nitriding process. This phenomenon resulted in the formation of a dual layer S phase, viz., a nitriding S phase on the outside and a carburizing S phase inside. The thickness of the S phase produced by the continuous process was similar to that generated by the single carburizing process.

(3) The average Vickers hardness of the S phase at the surface was 1210–1365 HV, and significant differences were not observed for different tungsten carbide compositions or plasma process conditions. On the other hand, the surface hardness profile of the S phase resulting from the continuous process at 450 °C was harder than that produced by the single carburizing process up to a depth of approximately 4 μm.

(4) The anodic polarization curves, obtained in a NaCl solution, show that the corrosion current densities of the plasma-processed layers are slightly lower than those of the as-deposited layers except for the 20 wt.% layer carburized at 450 °C. The pitting and crevice corrosion occurred in the as-deposited layers. The surface morphologies of the S phase after the anodic polarization measurements exhibited slight discoloration. However, no sever corrosion was observed in the plasma-processed layers implying that the carburizing and nitriding S phase exhibited comparable corrosion resistance enhancements.

(5) The results confirm that the single plasma carburizing process and continuous plasma process nitriding after carburizing at 400 and 450 °C improved the surface hardness and corrosion resistance of the composite layers. However, the metallurgical structure was very different from that of ordinary stainless-steel plates. These plasma treatments can be used as surface modification methods for additive manufacturing stainless-steel-based tungsten carbide composites that can withstand harsh environments.

Author Contributions: Conceptualization, S.A.; methodology, S.A.; investigation, S.A., T.Y., K.T., T.N. and N.U.; resources, S.A.; data curation, S.A.; formal analysis, S.A.; writing—original draft preparation, S.A.; writing—review and editing, S.A.; visualization, S.A.; supervision, S.A.; project administration, S.A.; funding acquisition, S.A. All authors have read and agreed to the published version of the manuscript.

Funding: This research was funded by JSPS KAKENHI (grant number: 18K04792).

Data Availability Statement: The data are available on request from the corresponding author.

Conflicts of Interest: The authors declare no conflict of interest.

References

1. Gnaase, S.; Niggemeyer, D.; Lehnert, D.; Bödgerand, C.; Tröster, T. Comparative Study of the Influence of Heat Treatment and Additive Manufacturing Process (LMD & L-PBF) on the Mechanical Properties of Specimens Manufactured from 1.2709. *Crystals* **2023**, *13*, 157. [CrossRef]
2. Kaligar, A.B.; Kumar, H.A.; Ali, A.; Abuzaid, W.; Egilmez, M.; Alkhader, M.; Abed, F.; Alnaser, A.S. Femtosecond Laser-Based Additive Manufacturing: Current Status and Perspectives. *Quantum Beam Sci.* **2022**, *6*, 5. [CrossRef]
3. Ladani, L.; Sadeghilaridjani, M. Review of Powder Bed Fusion Additive Manufacturing for Metals. *Metals* **2021**, *11*, 1391. [CrossRef]
4. Dass, A.; Moridi, A. State of the Art in Directed Energy Deposition: From Additive Manufacturing to Materials Design. *Coatings* **2019**, *9*, 418. [CrossRef]
5. Singh, A.; Kapil, S.; Das, M. A comprehensive review of the methods and mechanisms for powder feedstock handling in directed energy deposition. *Addit. Manuf.* **2020**, *35*, 101388. [CrossRef]
6. Li, N.; Huang, S.; Zhang, G.; Qin, R.; Liu, W.; Xiong, H.; Shi, G.; Blackburn, J. Progress in additive manufacturing on new materials: A review. *J. Mater. Sci. Technol.* **2019**, *35*, 242–269. [CrossRef]
7. Ligabo, S.A.; Braga, V.; Ferreira, C.C.A.; Siqueira, R.H.M.; Lourenço, J.C.; Abdalla, A.J.; Lima, M.S.F. Microstructure and Corrosion Behavior of AISI 316 Steel Layers Deposited on AISI 347 Steel Substrate by Laser Metal Deposition. *Metals* **2022**, *12*, 2161. [CrossRef]
8. Zinovieva, O.; Romanova, V.; Balokhonov, R. Effects of scanning pattern on the grain structure and elastic properties of additively manufactured 316L austenitic stainless steel. *Mater. Sci. Eng. A* **2022**, *832*, 142447. [CrossRef]
9. Avanzini, A. Fatigue Behavior of Additively Manufactured Stainless Steel 316L. *Materials* **2023**, *16*, 65. [CrossRef]
10. Haghdadi, N.; Laleh, M.; Moyle, M.; Primig, S. Additive manufacturing of steels: A review of achievements and challenges. *J. Mater. Sci.* **2021**, *56*, 64–107. [CrossRef]
11. Bajaj, P.; Hariharan, A.; Kini, A.; Kürnsteiner, P.; Raabe, D.; Jägle, E.A. Steels in additive manufacturing: A review of their microstructure and properties. *Mater. Sci. Eng. A* **2020**, *772*, 138633. [CrossRef]
12. Röttger, A.; Boes, J.; Theisen, W.; Thiele, M.; Esen, C.; Edelmann, A.; Hellmann, R. Microstructure and mechanical properties of 316L austenitic stainless steel processed by different SLM devices. *J. Adv. Manuf. Technol.* **2020**, *108*, 769–783. [CrossRef]
13. Bassis, M.; Ron, T.; Leon, A.; Kotliar, A.; Kotliar, R.; Shirizly, A.; Aghion, E. The Influence of Intralayer Porosity and Phase Transition on Corrosion Fatigue of Additively Manufactured 316L Stainless Steel Obtained by Direct Energy Deposition Process. *Materials* **2022**, *15*, 5481. [CrossRef] [PubMed]
14. Fetni, S.; Enrici, T.M.; Niccolini, T.; Tran, S.H.; Dedry, O.; Jardin, R.; Duchene, L.; Mertens, A.; Habraken, A.M. 2D thermal finite element analysis of laser cladding of 316L + WC composite layer coatings. *Procedia Manuf.* **2020**, *50*, 86–92. [CrossRef]

15. Enrici, T.M.; Dedry, O.; Boschini, F.; Tchuindjang, J.T.; Mertens, A. Microstructural and thermal characterization of 316L + WC composite layer coatings obtained by laser cladding. *Adv. Eng. Mater.* **2020**, *22*, 2000291. [CrossRef]
16. Fetni, S.; Enrici, T.M.; Niccolini, T. Thermal model for the directed energy deposition of composite layer coatings of 316L stainless steel enriched with tungsten carbides. *Mater. Des.* **2021**, *204*, 109661. [CrossRef]
17. Benarji, K.; Kumar, Y.R.; Jinoop, A.N.; Paul, C.P.; Bindra, K.S. Effect of WC Composition on the Microstructure and Surface Properties of Laser Directed Energy Deposited SS 316-WC Composite layers. *J. Mater. Eng. Perform.* **2021**, *30*, 6732–6742. [CrossRef]
18. Li, H.; Hu, Y.; Di, R.; Yuan, R.; Shi, C.; Lei, J. Effects of WC particles on microstructure and mechanical properties of 316L steel obtained by laser melting deposition. *Ceram. Int.* **2022**, *48*, 20388–20399. [CrossRef]
19. Borgioli, F. The "Expanded" Phases in the Low-Temperature Treated Stainless Steels: A Review. *Metals* **2022**, *12*, 331. [CrossRef]
20. Moskvina, V.; Maier, G.; Melnikov, E.; Astafurov, S.; Zagibalova, E.; Panchenko, M.; Reunova, K.; Nikolaev, A.; Ramazanov, K.; Astafurova, E. The effect of thin surface layer of nitrogen-expanded austenite on bulk γ-α′ phase transformation in low-temperature deformation of 316L stainless steel. *Mater. Lett.* **2021**, *304*, 130676. [CrossRef]
21. Borgioli, F.; Galvanetto, E.; Bacci, T. Surface Modification of a Nickel-Free Austenitic Stainless Steel by Low-Temperature Nitriding. *Metals* **2021**, *11*, 1845. [CrossRef]
22. Funch, C.V.; Somlo, K.; Christiansen, T.L.; Somers, M.A. Thermochemical post-processing of additively manufactured austenitic stainless steel. *Surf. Coat. Technol.* **2022**, *441*, 128495. [CrossRef]
23. Lindner, T.; Kutschmann, P.; Löbel, M.; Lampke, T. Hardening of HVOF-Sprayed Austenitic Stainless-Steel Coatings by Gas Nitriding. *Coatings* **2018**, *8*, 348. [CrossRef]
24. Adachi, S.; Egawa, M.; Yamaguchi, T.; Ueda, N. Low-temperature plasma nitriding for austenitic stainless steel layers with various nickel contents fabricated via direct laser metal deposition. *Coatings* **2020**, *10*, 365. [CrossRef]
25. Liu, Y.; Liu, D.; Zhang, X.; Li, W.; Ma, A.; Fan, K.; Xing, W. Effect of Alloying Elements and Low Temperature Plasma Nitriding on Corrosion Resistance of Stainless Steel. *Materials* **2022**, *15*, 6575. [CrossRef]
26. Borgioli, F. From Austenitic Stainless Steel to Expanded Austenite-S Phase: Formation, Characteristics and Properties of an Elusive Metastable Phase. *Metals* **2020**, *10*, 187. [CrossRef]
27. Borgioli, F.; Galvanetto, E.; Bacci, T. Effects of Surface Modification by Means of Low-Temperature Plasma Nitriding on Wetting and Corrosion Behavior of Austenitic Stainless Steel. *Coatings* **2020**, *10*, 98. [CrossRef]
28. Yazıcı, M.; Çomaklı, O.; Yetim, T.; Yetim, A.F.; Çelik, A. The effect of plasma nitriding temperature on the electrochemical and semiconducting properties of thin passive films formed on 316 L stainless steel implant material in SBF solution. *Surf. Coat. Technol.* **2015**, *261*, 181–188. [CrossRef]
29. Adachi, S.; Yamaguchi, T.; Ueda, N. Formation and Properties of Nitrocarburizing S-Phase on AISI 316L Stainless Steel-Based WC Composite Layers by Low-Temperature Plasma Nitriding. *Metals* **2021**, *11*, 1538. [CrossRef]
30. Savrai, R.A.; Skorynina, P.A. Structural-phase transformations and changes in the properties of AISI 321 stainless steel induced by liquid carburizing at low temperature. *Surf. Coat. Technol.* **2022**, *443*, 128613. [CrossRef]
31. Liu, H.Y.; Che, H.L.; Gao, J.Y.; Li, G.B.; Lei, M.K. Low-pressure hollow cathode plasma source carburizing of AISI 304L austenitic stainless steel at low temperature. *Surf. Coat. Technol.* **2022**, *442*, 128548. [CrossRef]
32. Montanari, R.; Lanzutti, A.; Richetta, M.; Tursunbaev, J.; Vaglio, E.; Varone, A.; Verona, C. Plasma Carburizing of Laser Powder Bed Fusion Manufactured 316 L Steel for Enhancing the Surface Hardness. *Coatings* **2022**, *12*, 258. [CrossRef]
33. Liu, Z.; Wang, S.; Zhang, S.; Feng, Y.; Peng, Y.; Gong, J. Deformation response of gradient low-temperature gaseous carburized case in austenitic stainless steel during cyclic nanoindentation. *Mater. Today Commun.* **2021**, *28*, 102714. [CrossRef]
34. Maistro, G.; Kante, S.; Nyborg, L.; Cao, Y. Low-temperature carburized high-alloyed austenitic stainless steels in PEMFC cathodic environment. *Surf. Interfaces* **2021**, *24*, 101093. [CrossRef]
35. Cheon, H.; Kim, K.S.; Kim, S.; Heo, S.B.; Lim, J.H.; Kim, J.H.; Yoon, S.Y. Effect of Deformation Structure of AISI 316L in Low-Temperature Vacuum Carburizing. *Metals* **2021**, *11*, 1762. [CrossRef]
36. Molleja, J.G.; Nosei, L.; Ferrón, J.; Bemporad, E.; Lesage, J.; Chicot, D.; Feugeas, J. Characterization of expanded austenite developed on AISI 316L stainless steel by plasma carburization. *Surf. Coat. Technol.* **2010**, *204*, 3750–3759. [CrossRef]
37. Adachi, S.; Ueda, N. Surface hardness improvement of plasma-sprayed AISI 316L stainless steel coating by low-temperature plasma carburizing. *Adv. Powder Technol.* **2013**, *24*, 818–823. [CrossRef]
38. Adachi, S.; Ueda, N. Combined plasma carburizing and nitriding of sprayed AISI 316L steel coating for improved wear resistance. *Surf. Coat. Technol.* **2014**, *259*, 44–49. [CrossRef]
39. Adachi, S.; Ueda, N. Wear and corrosion properties of cold-sprayed AISI 316L coatings treated by combined plasma carburizing and nitriding at low temperature. *Coatings* **2018**, *8*, 456. [CrossRef]
40. Azmi, F.; Basak, A.K.; Adenan, M.S.; Haruman, E.; Saedon, J.B. Responses of hybrid S phase layer to nanoscratching. *Surf. Coat. Technol.* **2022**, *441*, 128509. [CrossRef]
41. Ullah, N.; Naeem, M.; Shafiq, M.; Mujahid, Z.; Díaz-Guillén, J.C.; Lopez-Badillo, C.M.; Zakaullah, M. Effect of methane concentration on surface properties of cathodic cage plasma nitrocarburized AISI-304. *Appl. Phys.* **2021**, *127*, 529. [CrossRef]
42. Böcker, J.; Puth, A.; Dalke, A.; Röpcke, J.; Helden, J.P.H.; Biermann, H. Influence of the Active Screen Plasma Power during Afterglow Nitrocarburizing on the Surface Modification of AISI 316L. *Coatings* **2020**, *10*, 1112. [CrossRef]

43. Wu, D.; Ge, Y.; Kahn, H.; Ernst, F.; Heuer, A.H. Diffusion profiles after nitrocarburizing austenitic stainless steel. *Surf. Coat. Technol.* **2015**, *279*, 180–185. [CrossRef]
44. Scheuer, J.C.; Rodrigo, J.D.; Cardoso, P.; Sílvio, D.; Brunatto, F. Sequential low-temperature plasma-assisted thermochemical treatments of the AISI 420 martensitic stainless steel. *Surf. Coat. Technol.* **2021**, *421*, 127459. [CrossRef]
45. Lindner, T.; Mehner, T.; Lampke, T. Surface modification of austenitic thermal-spray coatings by low-temperature nitrocarburizing. *IOP Conf. Ser. Mater. Sci. Eng.* **2016**, *118*, 012008. [CrossRef]
46. Godec, M.; Donik, Č.; Kocijan, A.; Podgornik, B.; Skobir Balantič, D.A. Effect of post-treated low-temperature plasma nitriding on the wear and corrosion resistance of 316L stainless steel manufactured by laser powder-bed fusion. *Addit. Manuf.* **2020**, *32*, 101000–101008. [CrossRef]
47. Kovács1, D.; Kemény, D.M. Effect of plasma nitriding of austenitic stainless steel produced by direct metal laser sintering. *Acta Metall. Slovaca* **2021**, *27*, 190–194. [CrossRef]
48. Czerwiec, T.; He, H.; Weber, S.; Dong, C.; Michel, H. On the occurrence of dual diffusion layers during plasma-assisted nitriding of austenitic stainless steel. *Surf. Coat. Technol.* **2006**, *200*, 5289–5295. [CrossRef]
49. Micheler, T. Influence of plasma nitriding on hydrogen environment embrittlement of 1.4301 austenitic stainless steel. *Surf. Coat. Technol.* **2008**, *202*, 1688–1695. [CrossRef]
50. Ceschini, L.; Chiavari, C.; Lanzoni, E.; Martini, C. Low-temperature carburised AISI 316L austenitic stainless steel: Wear and corrosion behaviour. *Mater. Des.* **2012**, *38*, 154–160. [CrossRef]
51. Peng, Y.; Gong, J.; Chen, C.; Liu, Z.; Jiang, Y. Numerical Analysis of Stress Gradient and Traps Effects on Carbon Diffusion in AISI 316L during Low Temperature Gas Phase Carburization. *Metals* **2018**, *8*, 214. [CrossRef]
52. Ernst, F.; Li, D.; Kahn, H.; Michal, G.M.; Heuer, A.H. The carbide M_7C_3 in low-temperature-carburized austenitic stainless steel. *Acta Mater.* **2011**, *5*, 2268–2276. [CrossRef]
53. Christiansen, T.; Somers, M.A.J. Low temperature gaseous nitriding and carburising of stainless steel. *Surf. Eng.* **2005**, *21*, 445–455. [CrossRef]
54. Thaiwatthana, S.; Li, X.; Dong, H.B.; Bell, T. Comparison Studies on Properties of Nitrogen and Carbon S Phase on Low Temperature Plasma Alloyed AISI 316 Stainless Steel. *Surf. Eng.* **2002**, *18*, 433–437. [CrossRef]
55. Sun, Y. Hybrid Plasma Surface Alloying of Austenitic Stainless Steels with Nitrogen and Carbon. *Mater. Sci. Eng. A* **2005**, *404*, 124–129. [CrossRef]
56. Gu, X.; Michal, M.G.; Frank, E.; Kahn, H. Numerical Simulations of Carbon and Nitrogen Composition Depth Profiles in Nitrocarburized Austenitic Stainless Steels. *Metall. Mater. Trans. A* **2014**, *45A*, 4268–4279. [CrossRef]
57. Buhagiar, J.; Spiteri, A.; Sacco, M.; Sinagra, E.; Dong, H. Augmentation of crevice corrosion resistance of medical grade 316LV stainless steel by plasma carburizing. *Corros. Sci.* **2012**, *59*, 169–178. [CrossRef]
58. Borgioli, F. The Corrosion Behavior in Different Environments of Austenitic Stainless Steels Subjected to Thermochemical Surface Treatments at Low Temperatures: An Overview. *Metals* **2023**, *13*, 776. [CrossRef]

Disclaimer/Publisher's Note: The statements, opinions and data contained in all publications are solely those of the individual author(s) and contributor(s) and not of MDPI and/or the editor(s). MDPI and/or the editor(s) disclaim responsibility for any injury to people or property resulting from any ideas, methods, instructions or products referred to in the content.